Giant orbital Zeeman effects in a magnetic topological van der Waals interphase

Tobias Wichmann, ^{1,2,3} Mirco Sastges, ^{4,5,6} Keda Jin, ^{1,2,7} Jose Martinez-Castro, ^{1,2,7} Tom G. Saunderson, ^{4,5} Dongwook Go, ^{5,9} Honey Boban, ⁸ Samir Lounis, ¹⁰ Lukasz Plucinski, ⁸ Markus Ternes, ^{1,2,7} Yuriy Mokrousov, ^{4,5} F. Stefan Tautz^{1,2,3} and Felix Lüpke^{1,2,11,*}

¹Peter Grünberg Institute (PGI-3), Forschungszentrum Jülich, 52425 Jülich, Germany
²Jülich Aachen Research Alliance, Fundamentals of Future Information Technology, 52425 Jülich, Germany
³Institut für Experimentalphysik IV A, RWTH Aachen University, 52074 Aachen, Germany
⁴Institute of Physics, Johannes Gutenberg University, 55099 Mainz, Germany
⁵Peter Grünberg Institute (PGI-1), Forschungszentrum Jülich, 52425 Jülich, Germany
⁶Department of Physics, RWTH Aachen University, 52056 Aachen, Germany
⁷Institut für Experimentalphysik II B, RWTH Aachen University, 52074 Aachen, Germany
⁸Peter Grünberg Institute (PGI-6), Forschungszentrum Jülich, 52425 Jülich, Germany
⁹Department of Physics, Korea University, Seoul 02841, Republic of Korea
¹⁰Institute of Physics and Halle-Berlin-Regensburg Cluster of Excellence
CCE, Martin-Luther-University Halle-Wittenberg, 06099 Halle, Germany
¹¹Institute of Physics II, Universität zu Köln, Zülpicher Straβe 77, 50937 Cologne, Germany

*E-mail: f.luepke@fz-juelich.de

Van der Waals (vdW) heterostructures allow the engineering of electronic and magnetic properties by the stacking different two-dimensional vdW materials. For example, orbital hybridisation and charge transfer at a vdW interface may result in electric fields across the interface that give rise to Rashba spin-orbit coupling. In magnetic vdW heterostructures, this in turn can drive the Dzyaloshinskii–Moriya interaction which leads to a canting of local magnetic moments at the vdW interface and may thus stabilise novel 2D magnetic phases. While such emergent magnetic 'interphases' offer a promising platform for spin-based electronics, direct spectroscopic evidence for them is still lacking. Here, we report Zeeman effects with Landé g-factors up to ≈ 230 at the interface of graphene and the vdW ferromagnet Fe $_3$ GeTe $_2$. They arise from a magnetic interphase in which local-moment canting and itinerant orbital moments generated by the non-trivial band topology of Fe $_3$ GeTe $_2$ conspire to cause a giant asymmetric level splitting when a magnetic field is applied. Exploiting the inelastic phonon gap of graphene, we can directly access the buried vdW interface to the Fe $_3$ GeTe $_2$ by scanning tunnelling spectroscopy. Systematically analyzing the Faraday-like screening of the tip electric field by the graphene, we demonstrate the tunability of the constitutional interface dipole, as well as the Zeeman effect, by tip gating. Our findings are supported by density functional theory and electrostatic modelling.

The interplay of topological band structures and magnetism provides a rich playground for the realization of exotic materials [1–4]. This combination of properties may either be achieved by doping magnetism into topological matter, or by employing materials in which intrinsic magnetic order coexists with non-trivial band topologies. An example for the latter case is Fe₃GeTe₂ (FGT), a metallic vdW ferromagnet with a Curie temperature of $T_c \approx 220 \, \mathrm{K}$ in the bulk [5, 6]. While FGT's magnetic properties at temperatures $T \gtrsim T_c$ originate from localized Fe moments, for $T \ll T_c$ itinerant Stoner-like magnetism, carried by coherent delocalized Fe states, dominates [7-9]. In addition to its ferromagnetic properties, the band structure of FGT exhibits a topological nodal line gap that originates from a crossing of hybridized Fe-I and Fe-II spin-majority bands at its k = K/K' points (Ref. 10 and Fig. 1a-c). The band hybridization near this topological gap results in large Berry curvatures $\Omega(\mathbf{k})$ [10] and in turn orbital magnetic moments $\mathbf{m}(\mathbf{k}) \sim -\Omega(\mathbf{k})$ which dominate the spin moments at the edges of these bands (Fig. 1d). The interplay of strongly correlated itinerant magnetism and Fe local moments results in a large magnetic anisotropy energy [11–13] that allows to control the magnetic state of FGT not only by

external magnetic fields but also by charge-addressing stimuli, such as electric fields, currents and doping [11, 14–16]. This opens up the possibility to engineer magnetic properties at interfaces via the electric fields that arise when different materials are brought into contact, or even by external gates.

Here, we report a giant asymmetric Zeeman effect at the interface between monolayer graphene and FGT, which is moreover tunable by varying the interface dipole via electrostatic gating. A detailed analysis combining scanning tunnelling microscopy/spectroscopy (STM/STS) and theoretical calculations reveals that this unusual Zeeman effect is the result of two coupled orbital Zeeman effects: On the one hand, the band hybridization near the topological band gap results in localized out-of-plane band orbital moments (BOM) $m_z^{\rm BO}$ near the K/K' points. On the other hand, a canting of Fe local moments that has previously been reported in transport studies of graphene/FGT interfaces [13, 21] gives rise to chiral orbital moments (COM) $m_z^{\rm CO}$, which result from the winding of the itinerant charge carrier wave functions as they traverse the non-collinear texture of localized moments at the vdW interface and which can directly couple to external magnetic fields with large g-factors [22–27]. This complex compound Zee-

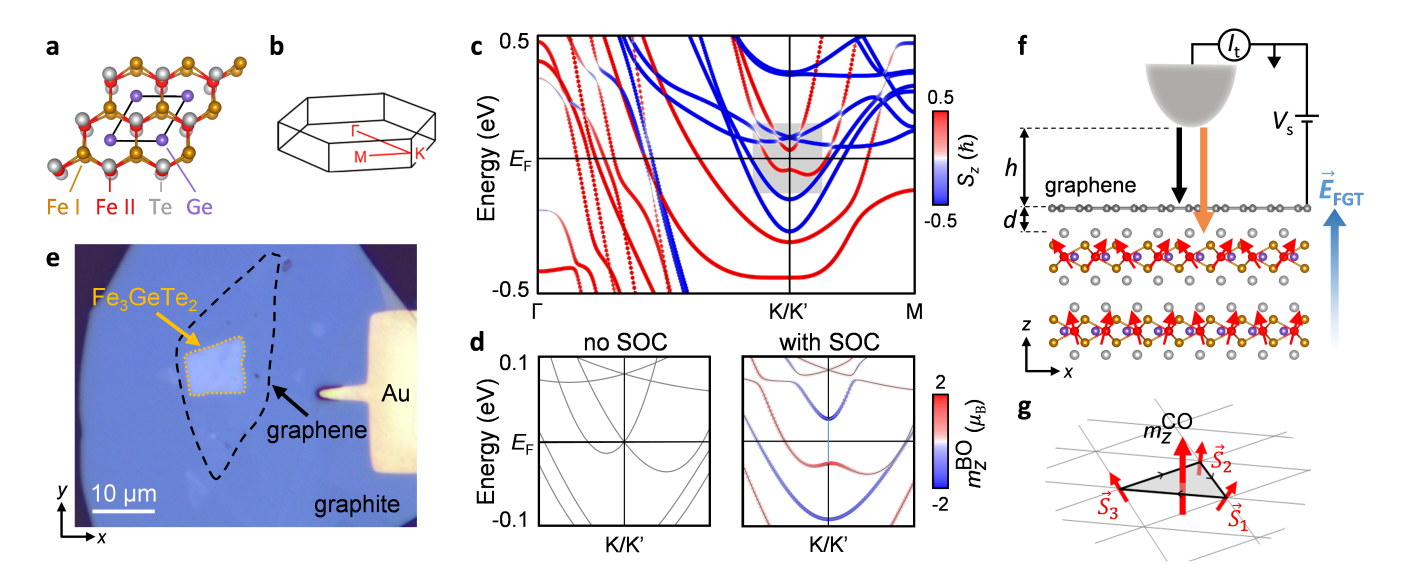


FIG. 1. Orbital moments in Fe₃GeTe₂ and scanning tunnelling microscopy experiment of the graphene/Fe₃GeTe₂ heterostructure. (a) Top view of the monolayer Fe₃GeTe₂ unit cell, highlighting the two inequivalent Fe sites. (b) First Brillouin zone of Fe₃GeTe₂ with indicated symmetry points and lines. (c) Spin-resolved band structure of bulk Fe₃GeTe₂, calculated by density functional theory including spin-orbit coupling, with color-coded majority (red) and minority (blue) bands. Near Γ only dispersive bands cross the Fermi energy E_F , while at K/K' several band extrema are located close to E_F . (d) Zoom into the shaded region in panel c, calculated without (left) and with (right) spin-orbit coupling. The latter calculation shows out-of-plane orbital magnetic moments $m_z^{\rm BO}$ near the K/K' points. (e) Optical micrograph of a graphene/Fe₃GeTe₂ heterostructure. Outlines of the respective flakes are indicated. (f) Schematic side view of the heterostructure and the scanning tunnelling microscopy setup. There are two parallel tunnelling channels, from the tip to graphene (black arrow) and to Fe₃GeTe₂ (orange arrow). The tip-sample distance h and graphene-Fe₃GeTe₂ distance h are indicated. h is the sample bias and h the tunnelling current. At the graphene/Fe₃GeTe₂ vdW interface, a charge transfer dipole gives rise to an internal electric field h interface (indicated by the red arrows at the Fe-II sites), due to the Rashba effect and Dzyaloshinskii–Moriya interaction (see main text for details). (g) Schematic of non-collinear spin arrangement in the Fe-I sublattice, where a canting of localized spins h in a conical spin structure. The ensuing scalar spin chirality gives rise to a chiral orbital moment h in h

man effect signals the emergence of subtle correlations between magnetic and topological electronic properties, which may open up the opportunity to engineer the response of the heterostructure to magnetic and electric fields, e.g., for chiral orbitronics applications.

RESULTS

The graphene/FGT heterostructure

An optical micrograph of a graphene/FGT heterostructure, a $28\,\mathrm{nm}$ thick FGT flake encapsulated between monolayer graphene on the top and an additional graphite flake underneath, is shown in Fig. 1e. For details of the sample fabrication see the Methods section. We note that the complete encapsulation of FGT by a larger graphene flake prevents the former's degradation. At this thickness and the experimental temperature of $\sim 6\,\mathrm{K}$, an isolated FGT flake would be in a single-domain ferromagnetic state [14, 28], however, the symmetry breaking and electric field at the interface to the graphene give rise to a Dzyaloshinskii–Moriya interaction, which cants the magnetic moments at the interface away from surface normal [13], as indicated schematically in the

sketch of the heterostructure and the tunnelling experiment in Fig. 1f. Constant-current STM topography images of the graphene/FGT heterostructure (Fig. 2a) show a superposition of the atomic lattice of graphene and a long-range modulation that is a characteristic feature of FGT: It stems from random disorder in the partially occupied Fe-II sites (see Fig. 2a in Ref. 12). In the corresponding Fourier transform (Fig. 2b), we observe sharp spots due to the graphene ($a_{\rm gr}=246\,{\rm pm}$) and the FGT lattices ($a_{\rm FGT}=399\,{\rm pm}$), as well as their Moiré pattern ($a=524\,{\rm pm}$), indicating an atomically clean vdW interface. The relative orientation of both lattices is approximately 17° and can be visualized by respective Fourier filtering of the topography images (see Extended Data Fig. S1).

The inelastic tunnelling gap of graphene

Tunnelling spectra recorded on the heterostructure reveals the characteristic V-shaped density of states of the graphene Dirac cone (Fig. 2c), as well as an inelastic tunnelling gap at the Fermi energy $E_{\rm F}$ ($eV_{\rm s}=0$). This gap results from a suppression of the tunnelling probability due to a momentum mismatch between the tunnelling tip and the finite parallel momenta of the graphene Dirac states at the

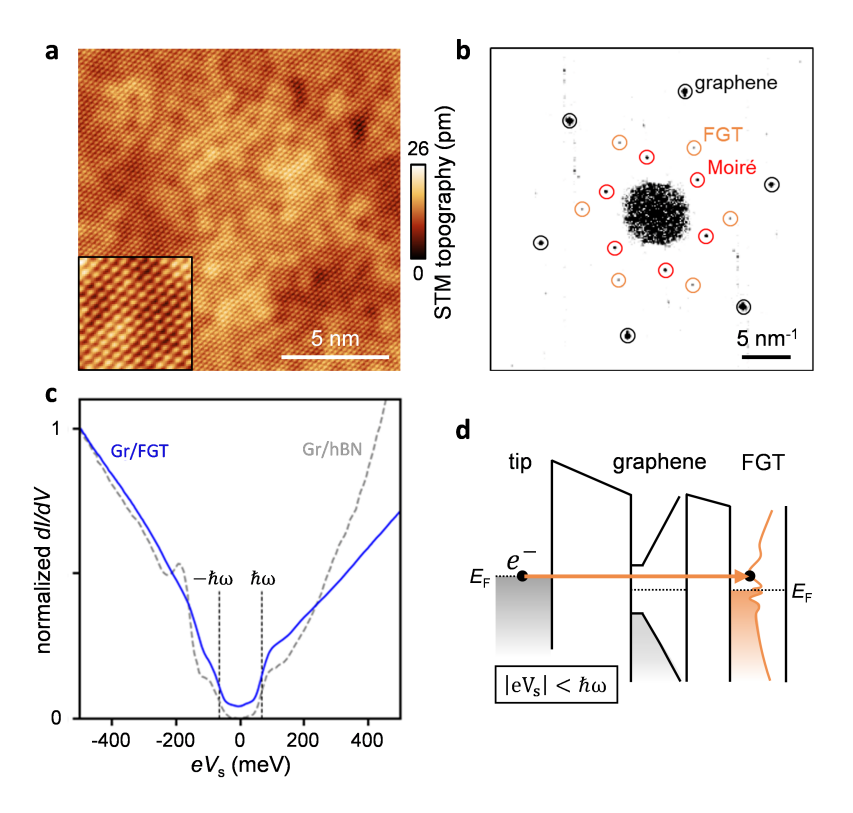


FIG. 2. Tunnelling through the inelastic gap of graphene. (a) STM topography of the graphene/Fe₃GeTe₂ heterostructure surface $(V_s = -50 \,\mathrm{mV}, \, I_t = 70 \,\mathrm{pA})$, simultaneously revealing atomic resolution of the graphene lattice and a longer-range modulation stemming from the partial occupancy of the Fe-II sites in Fe₃GeTe₂. Inset: Zoom into the graphene lattice (scan size $2.5 \,\mathrm{nm}$). (b) Fourier transform of the topography in panel a. The hexagonal patterns of graphene (black circles), Fe₃GeTe₂ (orange circles), and their moiré pattern (red circles) are clearly visible. (c) Spatially averaged tunnelling spectrum of the heterostructure (blue solid line, $V_s = 500 \,\mathrm{mV}$, $I_t = 200 \,\mathrm{pA}$). Below the inelastic threshold, i.e., for $|eV_s| < \hbar \omega$ where ω is a typical phonon frequency of graphene, an inelastic tunnelling gap is observed (vertical dotted lines), while outside this range the linear dispersion of the graphene Dirac cone is visible. Within the inelastic gap, a significant conductivity is measured, in contrast to the findings for graphene/hBN heterostructures (grey dashed line, data from Ref. [29]). The graphene is close to charge neutrality in both cases. For better comparison, both data sets are normalized at $eV_s = -500 \,\mathrm{meV}$. (d) Schematic diagram of the tunnelling processes. With its gapless spectrum, Fe₃GeTe₂ dominates the tunnelling current within the inelastic gap of the graphene.

K/K' points [29, 30]. However, above a threshold energy, i.e., for $|eV_s| \ge \hbar\omega = (65 \pm 2) \,\mathrm{meV}$ (Extended Data Fig. S2), phonon-assisted tunnelling channels become available, which significantly enhance the tunnelling probability. Our observed onset energy of the inelastic tunnelling channels corresponds to the lowest-energy graphene phonon mode [31], in good agreement with the phonon thresholds reported for graphene on different substrates [29, 30, 32]. This agreement indicates that the graphene is neither significantly strained nor strongly doped [30]. However, in contrast to graphene on insulating substrates, where the dI/dV signal almost vanishes below the phonon threshold [29-31, 33], we observe a significant tunnelling conductance for $|eV_s| < \hbar\omega$. The reason is that, while tunnelling to the graphene is suppressed in this energy range, charge carriers can still tunnel between the tip and the metallic FGT underneath the graphene, which allows us to directly access the electronic properties at the graphene/FGT interface (Fig. 2d).

Giant asymmetric Zeeman effect

A careful analysis of the tunnelling spectrum inside the inelastic phonon gap of graphene reveals two peaks, which strengthen on application of a magnetic field (Fig. 3a). At the same time, the linear Dirac spectrum of graphene outside the inelastic tunnelling gap remains mostly unaffected. Strikingly, the two peaks within the inelastic gap show significant energy shifts as function of the magnetic field. Linear fits to the data result in $g_1\mu_{\rm B}=(1.8\pm0.3)\,{\rm meV/T}$ and $g_2\mu_{
m B}=(13.3\pm0.4)\,{
m meV/T},$ corresponding to Landé gfactors $g=E_{\rm Zeeman}/(\mu_{\rm B}B)$ of $g_1\approx 30$ and $g_2\approx 230$, respectively (Fig. 3b and Extended Data Fig. S3). Furthermore, a spatial analysis of the peaks shows that they are consistent across the heterostructure surface and not localized at defects (Extended Data Fig. S4), pointing to a band-structure origin of of these features. Considering the FGT band structure, the observed peaks can be intuitively understood to stem from the flat band edges near the topological gap at the K/K' points, where the orbital magnetic moments $m_z^{\rm BO}$, concen-

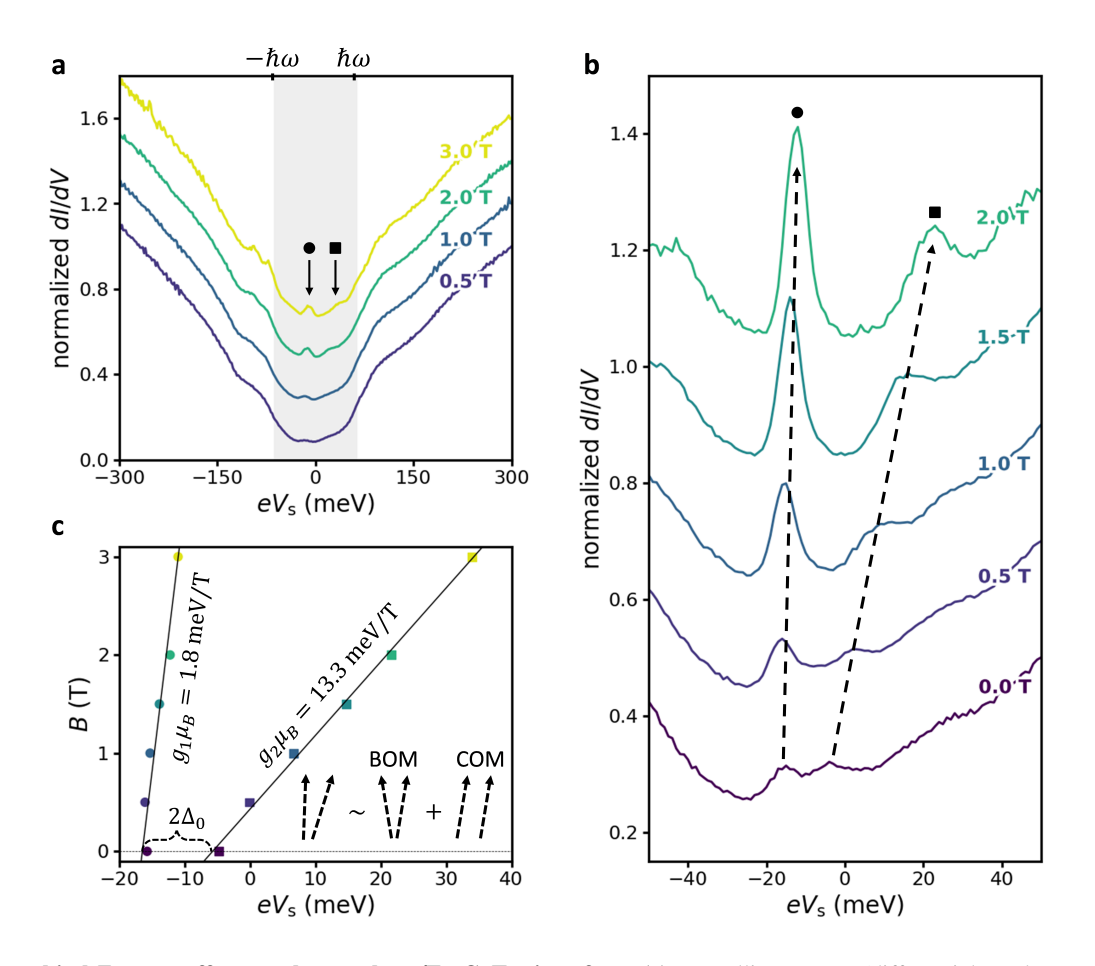


FIG. 3. Giant orbital Zeeman effects at the graphene/Fe₃GeTe₂ interface. (a) Tunnelling spectra (differential conductance in arbitrary units) for different out-of-plane B fields (normal to surface). For clarity, curves are offset by 0.2 arb. units each. In the inelastic gap of graphene (shaded region), two peaks emerge with increasing B field, as indicated by arrows and symbols. Tip stabilization parameters: $V_s = 300 \,\mathrm{mV}$ and $I_t = 1 \,\mathrm{nA}$. (b) Zoom into the inelastic-gap region, revealing both a continuous increase of the two peaks' intensities and shifts to higher energy as a function of applied B field. Curves are offset by 0.2 arb. units each. Dashed arrows are guides to the eye. Tip stabilization parameters: $V_s = 50 \,\mathrm{mV}$ and $I_t = 0.5 \,\mathrm{nA}$. (c) Symbols: Peak positions (horizontal axis) as function of applied B field (vertical axis). The solid lines are linear fits, yielding effective Landé g-factors $g_1 \approx 30$ (circles) and $g_2 \approx 230$ (squares). Inset: Schematic decomposition of the observed peak shifts into a splitting and a shifting contribution. The former arises from the band orbital moments (BOM) induced by the topological nodal line gap, while the latter has its origin in the chiral orbital moments (COM) induced by spin canting. For more details, see main text.

trated at the band extrema, lead to large g-factors (Fig. 1 and Refs. 26 and 34). This interpretation also explains the increasing peak intensity and sharpness with increasing magnetic field in Fig. 3b, analyzed in detail in Extended Data Fig. S3: DFT calculations show opposite orbital moments at the two band edges (Fig. 1d), such that the topological gap increases as function of the applied magnetic field. Concurrently, the band edges at K/K' flatten out further, again because the orbital magnetic moment is concentrated at the band extrema (Fig. 1c, d and Refs. [26, 34]). Extracting the splitting of the two peaks at B=0 results in $2\Delta_0=(10.8\pm0.7)\,\mathrm{meV}$, which agrees reasonably well with our DFT calculated spin orbit gaps at K/K' of $\sim 52 \,\mathrm{meV}$ and Refs. [10, 11], considering that the gap size decreases when inversion symmetry is broken (Extended Data Fig. S5). Note that the smaller the gap at B=0, the larger the orbital moments $m_z^{\rm BO}\sim \Delta^{-1}$ at K/K'

(see Methods section and Ref. 35).

While the model of opposite orbital moments $m_z^{\rm BO}$, concentrated at the upper and lower band edges, respectively, qualitatively explains both the observation of large g factors and of tunneling conductance peaks with increasing intensity and sharpness as the magnetic field is turned up, it disagrees with our experimental observations in that it would predict a B-field-induced shift of these conductance peaks in oppo-site directions, whereas we find that the peaks move in the same direction (to higher energy), albeit with different slopes (Fig. 3c). We therefore conclude that, in addition to the band orbital effect, there must be a second Zeeman effect at play which shifts both conductance peaks to higher energies, as schematically shown in the inset in Fig. 3c. Considering the band structure of FGT, such an effect is indeed expected, because the bands forming the topological gap exhibit the same

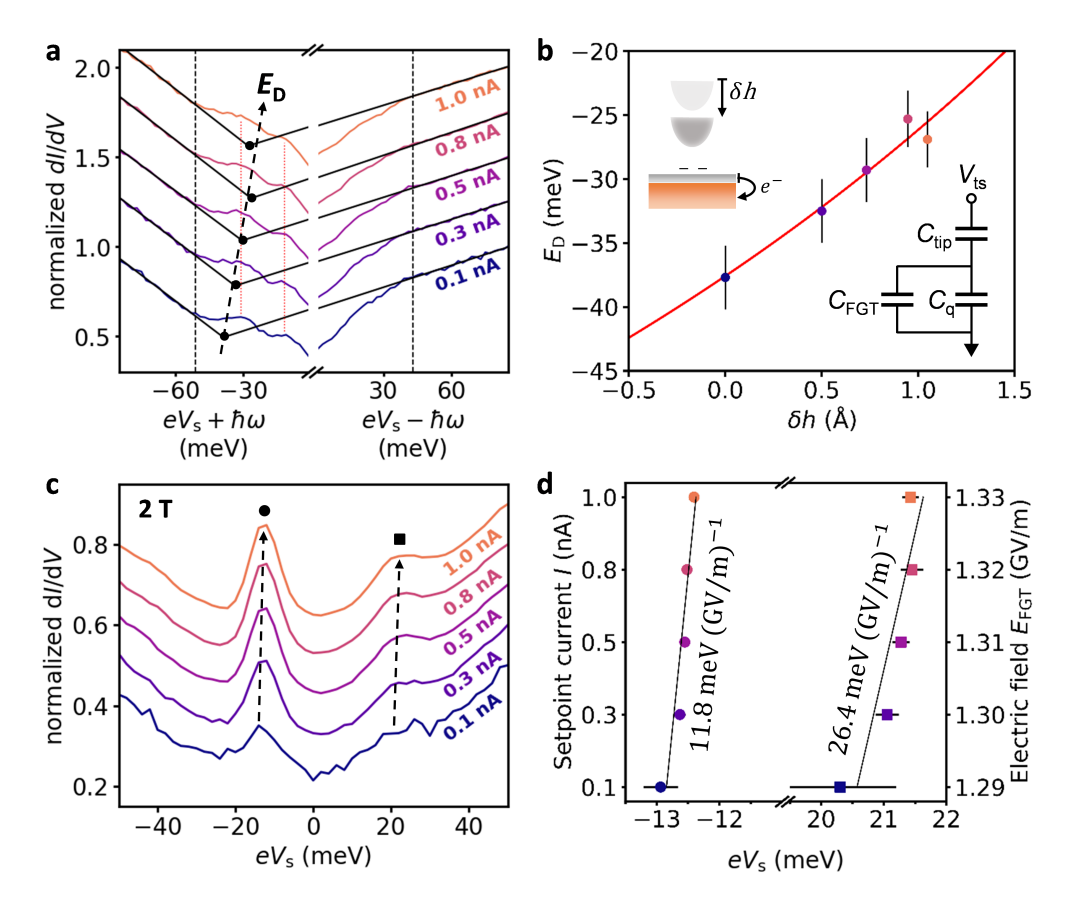


FIG. 4. Tuning the orbital Zeeman effects at the graphene/Fe₃GeTe₂ interface by electric fields. (a) Differential conductance spectra (in arbitrary units) for different tunnelling setpoints. The inelastic gap is cut out, and the curves for different setpoints are offset vertically for clarity. The Dirac point energy $E_{\rm D}$ (black dots) is extracted from the crossing points of line fits to the linear graphene spectrum above/below the vertical dashed lines, revealing a shift to higher values as the setpoint is increased. The dashed arrow is a guide to the eye. Remnant features due to Fe₃GeTe₂ near the edge of the inelastic gap do not shift with setpoint, as indicated by red dotted lines. The tip stabilization voltage was $V_{\rm s}=150\,{\rm mV}$ for all setpoints. (b) Dirac point energies $E_{\rm D}$ (filled circles, extracted from panel (a)) plotted as function of the change in tip-sample distance δh (see upper inset). Error bars are propagated from the fits of the Dirac spectrum in panel (a). The red curve is a fit to the data points, using the capacitor model in the lower inset (Eqs. 20 and 21 in the Methods section). (c) Differential conductance spectra (in arbitrary units) of the Fe₃GeTe₂-derived peaks in the inelastic gap of graphene for different tunnelling setpoints (curves are vertically offset for clarity. All spectra are recorded at a fixed external field of $B=2\,{\rm T}$. (d) Energy positions of the peaks in panel c as a function of setpoint current (Extended Data Fig. S8).

spin polarization (Fig. 1c, Extended Data Fig. S6). However, including the corresponding spin Zeeman effect, the combined g-factor of BOM and the band's spins at K/K' is only $g_z^{\rm BO}=|2+\langle L\rangle/\langle S\rangle|\lesssim 10$ (Ref. 36 and Extended Data Fig. S7), where $\langle L\rangle\sim 3\,\hbar$ and $\langle S\rangle\sim 0.5\,\hbar$ are taken from our DFT calculations, corresponding to shifts of $\sim 0.6\,{\rm meV/T}.$ Thus, the expected Zeeman effect purely based on FGT's spin and orbital band magnetism is much too small to explain the experimental observations in Fig. 3.

At this point, we recall that the local Fe moments at the graphene/FGT interface are canted (Fig. 1f), which is not included in the DFT calculations. The reason for the canting is the electric field perpendicular to the interface between the two vdW layers, which gives rise to a Rashba spin-orbit coupling and thus Dzyaloshinskii–Moriya interaction (DMI), which acts on the localized moments of primar-

ily Fe-I $3d_{x^2-y^2/xy}$ orbitals [9, 13, 21]. The Rashba coefficient at the graphene/FGT interface was theoretically estimated as $\alpha_{\rm R}\approx 246\,{\rm meV}$ Å, giving rise to a DMI strength of $|\vec{D}|=0.089\,{\rm meV}$ per unit cell [13], which we expect to be a lower bound for our experiments, because of an enhancement of the interface dipole by the tip compared to experiments discussed in the literature — see the next section. While at intermediate temperatures $10\,{\rm K} < {\rm T} < 220\,{\rm K}$, this effect leads to skyrmion formation [13], at our lower experimental temperatures we most likely stabilize a conical phase [37, 38], as schematically shown in Fig. 1f, g.

The un-canting of local moments by the application of an out-of-plane magnetic field is expected to ultimately result in the moments being aligned out-of-plane. However, to fully align the moments fields much larger than $0.089\,\mathrm{meV}/\mu_\mathrm{B}\gtrsim1.5\,\mathrm{T}$ (Ref. [13]) must be applied, which are not accessible in

our experiment. Also, it cannot explain the observed large g-factor of the Zeeman effect in Fig. 3c, because when the moments are canted away from the surface normal and thus are no longer aligned with the B field, their Zeeman effect is weakened instead of enhanced. Instead, we propose that the winding of the charge carrier wave functions of the spinpolarized bands that form the topological gap, as they traverse the non-collinear magnetic texture at the vdW interface, gives rise to chiral orbital moments (COM), which are described in detail in the literature [17–20, 23, 24, 27, 39]. In our system, since the bands in question have identical spin polarization, we expect any local-moment canting-induced COM to affect both bands in the same way, i.e., result in a Zeeman effect which shifts both bands to higher energy as we increase the magnetic field (inset Fig. 3c). Crucially, the canting, and consequently the COMs, are the result of the Rashba effect and the resulting DMI at the graphene/FGT interface. Thus, the resulting giant Zeeman effect should be tunable by variation of the electric field across the interface, which we demonstrate in the following.

Electric field tunability of the Zeeman effect

From simple electrostatic considerations, we estimate the electric field at the graphene/FGT interface as

$$E_{\text{FGT}} \equiv \vec{E}_{\text{FGT}} \cdot \hat{z} = (\Phi_{\text{gr}} - \Phi_{\text{FGT}})/ed \approx 1.41 \,\text{GV/m}, (1)$$

with the interlayer distance between graphene and FGT $d=3.34\,\mathrm{\mathring{A}}$ (Fig. 1f), the elementary charge e, the work function of FGT $\Phi_{\mathrm{FGT}}\approx 4.08\,\mathrm{eV}$ [40], and $\Phi_{\mathrm{gr}}=\Phi_{\mathrm{gr}}^0\approx 4.55\,\mathrm{eV}$ [41] the work function of charge-neutral graphene, respectively. However, when the heterostructure is initially assembled, the work function difference between graphene and FGT gives rise to a charge transfer (electrons flow from the low-work function FGT to the high-work function graphene), resulting in an intrinsically interface-driven n doping of the graphene and a corresponding shift of the Dirac point energy E_{D}^0 relative to the Fermi level, and thus the graphene work function becomes $\Phi_{\mathrm{gr}}=\Phi_{\mathrm{gr}}^0+E_{\mathrm{D}}^0$, where E_{D}^0 is a priori unknown. In addition to the interface-driven doping, the pres-

In addition to the interface-driven doping, the presence of the STM tip with its own distinct work function $(\Phi_{\rm tip} \approx 4.85\,{\rm eV})$, see Methods section) should affect $E_{\rm D}$ due to tip gating (clearly, also the applied bias voltage will contribute to a polarity-dependent gating; however, for bias voltages within the inelastic gap of graphene this effect is so small that it can be neglected). In Fig. 4a, tunnelling spectra recorded at different setpoints and therefore different tip heights h are plotted. Fitting the linear graphene spectrum outside of the inelastic gap to extract the setpoint-dependent Dirac point energy $E_{\rm D}$ from the crossing points of the linear fits (Fig. 4a and Extended Data Table I), we observe a shift of $E_{\rm D}$ to more positive values as h decreases. This corresponds to the graphene becoming less electron-doped as the tip is brought closer to the sample surface. In contrast, additional FGT features that are located outside the inelastic gap

of graphene show no sign of shifting as function of the setpoint current, demonstrating that mainly the graphene doping level is changed by the tip gating (Fig. 4a).

In order to determine the intrinsic doping level of graphene at the interface to FGT, we model the experimental tip-sample geometry by a capacitor circuit (lower inset in Fig. 4b and Methods section), which we fit to the experiment. Extrapolating this model to $\delta h \to -\infty$, i.e., to the absence of the tunnelling tip, we find a graphene doping level of $E_{\rm D}^0 =$ $-(579 \pm 171)\,\mathrm{meV}$ (Fig. 4b). The corresponding intrinsic electric field at the graphene/FGT interface is $E_{\rm FGT} =$ $(-0.3 \pm 0.5) \,\mathrm{GV/m}$, i.e., lower and of opposite sign compared to charge-neutral graphene and FGT. We note that a non-zero field is the prerequisite for the anomalous Hall effects and giant magnetoresistances at the graphene/FGT interface reported in the literature [13, 42]. In comparison, in the presence of the STM tip the interfacial electric field is significantly larger, in the range $E_{\rm FGT}=1.29$ to $1.32\,{\rm GV/m}$ for tunnelling setpoints $0.1-1\,\mathrm{nA}$ (see Extended Data Table 1) and thus also the DMI is expected to be larger.

To demonstrate that the variation of the interfacial electric field leads to a variation of the Rashba splitting and DMI, we study the peak positions inside the inelastic gap as function of tunnelling setpoint while keeping $B = 2 \,\mathrm{T}$ fixed (Fig. 4c). Doing so, we find an increase in the intensity of both peaks as we bring the tip closer to the sample surface. Such behaviour is a known effect for tunnelling into sharp energy levels originating from states with finite in-plane momenta, such as flat bands and localized states at K/K' [11, 43-45], which again is consistent with our DFT calculations. More interestingly though, extracting the precise peak positions as function of the tunnelling setpoint once more reveals systematic energy shifts (Fig. 4d and Extended Data Fig. S8). Linear fits to the data (solid lines in Fig. 4d) are described by $eV_{\rm s}=(11.8\pm$ $2.8) \,\mathrm{meV} \,(\mathrm{GV/m})^{-1} E_{\mathrm{FGT}} - (28.1 \pm 2.8) \,\mathrm{meV}$ and $eV_{\mathrm{s}} =$ $(26.4 \pm 8.1) \,\mathrm{meV} \,(\mathrm{GV/m})^{-1} E_{\mathrm{FGT}} - (13.5 \pm 10.6) \,\mathrm{meV},$ respectively. Remarkably, the peak positions show a qualitatively similar asymmetric splitting as function of E field at fixed B field, as they do for the increasing B field at fixed E field (Extended Data Fig. S9).

DISCUSSION

Our observed DMI-induced Zeeman effect indicates a strong inversion symmetry breaking at the graphene/FGT interface, evidenced by measurements on bulk FGT crystals, where no significant Zeeman effect is observed when the inversion symmetry is only weakly broken (Extended Data Fig. S10 and Ref. [11]). In general agreement with this interpretation, such symmetry breaking has recently been proposed as the origin of the anomalous Hall effect in graphene/FGT [46], which can be understood as the manifestation of the Zeeman effect in transport. Our observations imply that the band-structure-induced and chirality-induced moments are directly coupled beyond a mere superposition, which may explain the

enhancement of the BOM by more than one order of magnitude compared to the theoretical moments alone. Currently, the exact interaction mechanism between the chiral and band orbital moments is yet to be understood, but considering that both effects are closely related to the Berry curvature, it does not come as a surprise that they are coupled. Estimating the g-factors of the two contributions according to the inset in Fig. 3c results in $g_{\rm z}^{\rm BO} \approx 100$ and $g_{\rm z}^{\rm CO} \approx 130$, respectively, signifying their similar strength (see Methods section). In this context, we note that the spin Berry curvature vanishes for the band structures shown in Fig. 1c,d. However, spin canting likely leads to a finite spin Berry curvature, with similar localization at the K/K' points as the Berry curvature [34], which would couple the spin canting directly to the topological gap. Similar effects were recently reported in magnetic Kagome compounds, where the orbital moments of gapped Dirac cones interact with local moments [23, 26, 34, 47–50]. In the absence of spin canting, these bulk compounds can show spinorbit-driven orbital Zeeman effects [34, 48], which are initially approximately a linear function of the applied B field but saturate as the Berry curvatures decrease with increasing gap sizes. In the presence of spin canting, however, additional orbital moments with $q \gg 2$ were reported, due an interplay of the spin-orbit gap and spin chirality [22, 23, 25, 26]. However, in contrast to the Kagome compounds, where the Zeeman effects typically saturate at fields of $B\lesssim 2\,\mathrm{T}$, we do not observe any sign of a saturation at the graphene/FGT interface up to our maximum accessible field of 3 T, which is consistent with the spin un-canting at the graphene/FGT occuring only at much larger fields $B \sim 10 \, \mathrm{T}$.

CONCLUSION

In conclusion, despite the lack of strong bonding in graphene/FGT vdW heterostructures, interface dipoles give rise to emergent magnetoelectronic properties, which are localized at the 2D interface and result in a rich interplay of orbital magnetism and local moments. This "vdW interphase" provides a flexible platform to engineer magnetic properties, allowing to control them via gate-tuning the Rashba effect and DMI, which may find applications in spintronics or orbitronics.

METHODS

Density functional theory

The orbital magnetization in three-dimensional k-space is given by [22]

$$\mathbf{M}^{\mathrm{BO}} = \frac{e}{2\hbar} \mathrm{Im} \sum_{n} \int_{\mathrm{BZ}} \frac{d\mathbf{k}}{(2\pi)^{3}} f_{n\mathbf{k}} \langle \partial_{\mathbf{k}} u_{n\mathbf{k}} | \times \left(\hat{H}_{\mathbf{k}} + \varepsilon_{n\mathbf{k}} - 2\mu \right) \\ |\partial_{\mathbf{k}} u_{n\mathbf{k}} \rangle,$$

(2)

where $|u_{n\mathbf{k}}\rangle$ is the Bloch-like eigenstate associated with the n^{th} eigenvalue $\varepsilon_{n\mathbf{k}}$ of the Hamiltonian $H_{\mathbf{k}}$ of the system, $f_{n\mathbf{k}}$ is the zero-temperature Fermi occupation factor and μ the chemical potential. Note that the vector product is taken between the two derivatives $\partial_{\mathbf{k}} = \frac{\partial}{\partial \mathbf{k}}$ in the bra and ket, respectively.

Unlike transport, which probes all occupied states and is therefore sensitive to the orbital magnetization, STM/S probes the either filled or empty states at a given energy and is thus sensitive to the orbital magnetic moment (OMM) of the band, which is given by

$$m_n(\mathbf{k})^{\mathrm{BO}} = \frac{e}{2\hbar} \mathrm{Im} \langle \partial_{\mathbf{k}} u_{n\mathbf{k}} | \times \left(\hat{H}_{\mathbf{k}} - \varepsilon_{n\mathbf{k}} \right) | \partial_{\mathbf{k}} u_{n\mathbf{k}} \rangle.$$
 (3)

To calculate this quantity using ab initio methods, we performed the following procedure: The electronic structure of bulk Fe₃GeTe₂ was computed with the density functional theory code FLEUR [51] using the full-potential linearized augmented plane wave method [52]. We chose the Perdew-Burke-Ernzerhof exchange correlation functional within the generalized gradient approximation [53]. The lattice parameters for the system are [54] $a = 3.99 \,\text{Å}$ and $c = 16.33 \,\text{Å}$ in a hexagonal close-packed lattice. We performed a full self-consistent calculation to find the charge density including the effect of spin-orbit coupling within FLEUR, with a resulting magnetocrystalline anisotropy of 1.06 meV per Fe atom. The plane-wave cutoffs for the basis functions, for the charge density and for the exchange correlation functional were set to $5a_0^{-1}$, $15a_0^{-1}$, and $12.5a_0^{-1}$, respectively, where a_0 is the Bohr radius. For Fe and Ge, the maximum in the angular momentum expansion was set to $l_{\text{max}} = 8$ and the muffin-tin radii $r_{\rm MT}$ for both species was set to $2.12a_0$; for Te, $l_{\text{max}} = 10$ and $r_{\text{MT}} = 2.74a_0$. Despite previous work on FGT indicating the effects of strong electronic correlations [8, 12], in the present scenario we do not see indications of such correlations, e.g. as the conduction band minimum is moved through the Fermi energy, and thus did not consider them theoretically. Using the Wannier90 package [55, 56], from the DFT-calculated Bloch wave functions $|u_{n\mathbf{k}}\rangle$, we constructed maximally localised Wannier functions (MLWFs) and determine the Bloch-like basis $|u_{nk}^{W}\rangle$ [57, 58]. A mesh of $8 \times 8 \times 8$ k-points was used with 192 Bloch states to obtain 96 MLWFs. Initial projections were chosen to be d states for Fe and p states for Ge and Te atoms. The maximum frozen window was set to 2.344 eV above the Fermi energy. The Hamiltonian, spin, and orbital angular momentum (OAM) operators were evaluated in the Bloch basis and transformed into the MLWF basis. The OAM was integrated inside the muffin-tins. Further details of the calculations can be found in Refs. 59 and 60.

In the Wannier description, the orbital magnetization can be quantified as proposed by Lopez *et al.* [58]: First, the Blochlike basis $|u_{nk}^{W}\rangle$ is transformed into the so called Hamiltonian

gauge, using the transformation

$$|u_{n\mathbf{k}}^{\mathrm{H}}\rangle = \sum_{m}^{J} |u_{m\mathbf{k}}^{\mathrm{W}}\rangle U_{mn}\left(\mathbf{k}\right).$$
 (4)

This is necessary in order to compute the magnetization according to the so-called "modern theory of orbital magnetization" expression Eq. 2. This expression allowed us to decompose the orbital magnetization into its local

$$\mathbf{M}_{\mathrm{LC}}^{\mathrm{BO}} = \frac{e}{2\hbar} \mathrm{Im} \sum_{n} \int_{\mathrm{BZ}} \frac{d\mathbf{k}}{(2\pi)^{3}} f_{n\mathbf{k}} \langle \partial_{\mathbf{k}} u_{n\mathbf{k}}^{\mathrm{H}} | \times \left(\hat{H}_{\mathbf{k}} - \mu \right) | \partial_{\mathbf{k}} u_{n\mathbf{k}}^{\mathrm{H}} \rangle,$$
(5)

and itinerant contributions

$$\mathbf{M}_{\mathrm{IC}}^{\mathrm{BO}} = \frac{e}{2\hbar} \mathrm{Im} \sum_{n} \int_{\mathrm{BZ}} \frac{d\mathbf{k}}{(2\pi)^{3}} f_{n\mathbf{k}} \langle \partial_{\mathbf{k}} u_{n\mathbf{k}}^{\mathrm{H}} | \times (\varepsilon_{n\mathbf{k}} - \mu) | \partial_{\mathbf{k}} u_{n\mathbf{k}}^{\mathrm{H}} \rangle.$$
(6)

We computed the band-resolved contributions to the magnetization

$$m_{n,\text{LC}}^{\text{BO}} = \frac{e}{2\hbar} \text{Im} \langle \partial_{\mathbf{k}} u_{n\mathbf{k}}^{\text{H}} | \times \left(\hat{H}_{\mathbf{k}} - \mu \right) | \partial_{\mathbf{k}} u_{n\mathbf{k}}^{\text{H}} \rangle,$$
 (7)

and

$$m_{n,\text{IC}}^{\text{BO}} = \frac{e}{2\hbar} \text{Im} \langle \partial_{\mathbf{k}} u_{n\mathbf{k}}^{\text{H}} | \times (\varepsilon_{n\mathbf{k}} - \mu) | \partial_{\mathbf{k}} u_{n\mathbf{k}}^{\text{H}} \rangle.$$
 (8)

similar to Ref. 58, where it was shown that Eqs. 7 and 8 can be recast into a gauge-invariant formulation. A more detailed theoretical description will be presented in a forthcoming publication. Finally the orbital magnetic moments in Eq. 3 were determined from the k-resolved local and itinerant contributions as $m_n(\mathbf{k})^{\mathrm{BO}} = m_{n,\mathrm{LC}}^{\mathrm{BO}}(\mathbf{k}) - m_{n,\mathrm{IC}}^{\mathrm{BO}}(\mathbf{k})$.

We note at this point that an earlier proposed model of the relevant bands at K/K' [10], when inserted into Eq. 3, results in orbital moments which directly contradict our DFT calculations, indicating that such a model does not seem suitable to capture the full orbital physics.

Sample fabrication

Graphite and FGT crystals were exfoliated onto SiO₂ and assembled by a standard dry-transfer technique with a microdome polyvinylchlorid/polydimethylsiloxane (PVC/PDMS) stamp [61]. Ti/Au contacts were fabricated using maskless optical lithography, and samples were subsequently cleaned in an ambient-condition atomic force microscope by repeated scanning in contact mode over night. Extended Data Fig. S11 shows an AFM image, recorded before the STM measurements, of the heterostructure displayed in Fig. 1e. After introduction into the STM ultra-high vacuum chamber, the sample was annealed at 240°C for 15 mins to desorb residues and water and subsequently transferred to the STM. There, the sample was zero-field cooled to the

base temperature of $\sim 6.1\,\mathrm{K}$, and magnetized by ramping the surface-normal field to $B=2\,\mathrm{T}$, prior to STS measurements.

Graphite and Fe_3GeTe_2 were obtained from commercial sources (graphite from HQ graphene, FGT from 2D semi-conductors). FGT bulk crystals from the same batch were characterized by angle-resolved photoemission spectroscopy (ARPES), showing general agreement with the DFT calculations and literature, and a doping level for which E_F is close to the topological gap (Extended Data Fig. S12). STM/S spectra taken on the bulk crystals did not exhibit any peak features and virtually no magnetic field dependence (Extended Data Fig. S10), confirming the graphene/FGT interface as the source of the observed behaviour.

Scanning tunneling experiments

All STM/STS measurements were performed in a commercial Sigma Polar instrument at $\sim 6.1\,\mathrm{K}$. Electro-chemically etched W tips were annealed to orange glow in vacuum and prepared on an Ag(111) surface. After introducing the heterostructure sample to the STM scanner, we first approached the tip to the contact leads using visual control and then navigated the tip to the heterostructure by scanning. On the heterostructure, we performed large-area STM scans to locate the graphene and FGT flakes and to check the cleanliness of the heterostructure surface. To ensure a clean tunnelling spectrum, we then moved the tip back to the Ti/Au contact and safeguarded that it showed a linear I(V) characteristics by repeated careful indentation. We then retracted the tip out of tunnelling contact and jumped directly back to the clean surface of the heterostructure, where we performed the measurements, thus preventing any tip alterations that might have occured during intermediate scans. All spectroscopy measurements were performed after ramping the magnetic field above the saturation field of the FGT flake, to achieve a well-defined magnetization. STS was performed using standard lock-in techniques at a frequency of 877 Hz and modulation amplitudes of $V_s^{\text{mod}} = 1 \text{ to } 3 \text{ meV}$.

We extracted $E_{\rm D}$ in Fig. 4a from the V-shaped Dirac spectrum outside the inelastic gap, by (i) subtracting the energy offset resulting from the inelastic tunnelling process above the phonon threshold $\pm\hbar\omega$, for positive and negative bias voltages separately, and (ii) performing linear fits to the electron and hole sides of the linear Dirac cone spectrum, respectively; the Dirac point energy $E_{\rm D}$ at each setpoint current was then extracted from their intersection. To determine δh in Fig. 4, we used the exponential dependence of the tunnelling current on the tip-sample distance $I/I_0=\exp(\frac{h_0-h}{\lambda})$, where $\delta h=h_0-h$ and $\lambda^{-1}\approx(0.455\,{\rm \AA})^{-1}$ is the decay constant of the tunnelling current for monolayer graphene above the phonon threshold [30]. Then

$$\delta h = \lambda \ln(I/I_0),\tag{9}$$

which is independent of the absolute values of h and h_0 .

Electrostatic model

From the experimental geometry, we estimate the tip and FGT capacitance density with respect to the graphene as

$$C_{\rm tip} = \frac{\varepsilon_0}{h} \approx 0.88 \,\mu {\rm Fcm}^{-2}$$
 (10)

$$C_{\rm FGT} = \frac{\varepsilon_0}{d} \approx 2.651 \,\mu {\rm Fcm}^{-2},$$
 (11)

where ε_0 is the vacuum permittivity and we estimate a graphene/FGT layer spacing of $d=3.34\,\mathrm{\AA}$ and the initial tip height of $h=10\,\mathrm{\AA}$ at setpoint $V_\mathrm{s}=300\,\mathrm{mV}$, $I_0=0.1\,\mathrm{nA}$. We note that, realistically, the permittivity of the graphene/FGT interface is expected to be higher than ε_0 , which would result in an increase of C_FGT and thus a decrease of the electric field at the graphene/FGT interface. The finite screening length of the electric field in the FGT, on the other hand, leads to a decrease of C_FGT ; however, this change is expected to be small because of the metallic character of FGT and the resulting short screening length [62]. In any case, both of these effects have only minor influence on the tipheight dependence of the interface field in our study, because the response of the system is dominated by the change of the tip-sample capacitance C_tip .

To model the charge distribution across the junction and the heterostructure, we must take into account that the graphene screens the tip electric field from the FGT, similar to a Faraday screen [63]. We therefore employed a capacitor model of the junction similar to the one used in Ref. 64. Because of the low density of states of graphene close to the Dirac point, the model needs to include the graphene quantum capacitance (per unit sample area) [65]

$$C_{\mathbf{q}} = e^2 \rho, \tag{12}$$

where

$$\rho = \frac{2E_{\rm D}}{\pi(\hbar v_{\rm F})^2} \tag{13}$$

is the spin- and valley-degenerate graphene density of states at $E_{\rm F}$ (per unit sample area), and $v_{\rm F}$ the Dirac Fermi velocity. Integrating ρ from the Dirac point to $E_{\rm F}$, one obtains from Eq. 13 the number of carriers per unit area in graphene as $n_{
m gr}=\pi^{-1}(E_{
m D}/\hbar v_{
m F})^2.$ As usual, the quantum capacitance is implemented as a capacitor in series to the geometric capacitance between tip and graphene, $C_{\rm tip}$ (see inset Fig. 4b) [64]. As a result of the quantum capacitance, the tip electric field is not perfectly screened by the graphene and can penetrate to the FGT underneath, establishing a capacitance $C_{\rm FGT}$ between graphene and FGT, in series with $C_{\rm tip}$. Because it is equivalent to a single capacitor with distance h + d, the arrangement of $C_{
m tip}$ and $C_{
m FGT}$ in series is consistent with a tunneling path from the tip directly to the FGT. We thus have two parallel tunneling paths (the other one from the tip to graphene), which suggests putting the two capacitances C_{α} and $C_{\rm FGT}$ in parallel, both connected to the same back contact

of the Ti/Au substrate (within the metallic FGT layer, there will be no potential drop, despite its considerable thickness). In this model, we neglect the inhomogeneity of the electric field due to the curved tip shape, because we are interested only in the properties right underneath the tip apex and the small graphene-FGT distance compared to the tip radius (10 to $100\,\mathrm{nm}$) results in effectively parallel electric field lines there.

From the circuit diagram it is clear that

$$\frac{n_{\rm FGT}e}{C_{\rm FGT}} = \frac{n_{\rm gr}e}{C_{\rm q}} = \frac{n_{\rm tip}e}{C_{\rm tip}} - V_{\rm ts} \tag{14}$$

and

$$n_{\rm tip} + n_{\rm gr} + n_{\rm FGT} = 0, \tag{15}$$

the latter due to charge conservation, where $n_{\rm gr}$, $n_{\rm tip}$, and $n_{\rm FGT}$ are the areal charge densities on graphene and the surfaces of the tip and FGT, respectively. We solve the linear equation system by substituting expressions derived from Eq. 14 into Eq. 15, obtaining

$$n_{\rm gr} + \frac{C_{\rm tip}V_{\rm ts}}{e} + \frac{C_{\rm tip}}{C_{\rm q}}n_{\rm gr} + \frac{C_{\rm FGT}}{C_{\rm q}}n_{\rm gr} = 0. \tag{16}$$

Using the graphene quantum capacitance (Eqs. 13 and 12) [65]

$$C_{\rm q} = \frac{2e^2}{\sqrt{\pi(\hbar v_{\rm F})^2}} \sqrt{n_{\rm gr}},$$
 (17)

results in

$$n_{\rm gr} + (C_{\rm tip} + C_{\rm FGT}) \frac{\sqrt{\pi (\hbar v_{\rm F})^2}}{2e^2} \sqrt{n_{\rm gr}} + \frac{C_{\rm tip} V_{\rm ts}}{e} = 0.(18)$$

Substituting $a \equiv \frac{\sqrt{\pi(\hbar v_{\rm F})^2}}{2e^2}$ gives

$$n_{\rm gr} + a(C_{\rm tip} + C_{\rm FGT})\sqrt{n_{\rm gr}} + \frac{C_{\rm tip}V_{\rm ts}}{e} = 0, \qquad (19)$$

which yields

$$\sqrt{n_{\rm gr}} = -\frac{a(C_{\rm tip} + C_{\rm FGT})}{2} + \sqrt{\left(\frac{a(C_{\rm tip} + C_{\rm FGT})}{2}\right)^2 - \frac{C_{\rm tip}V_{\rm ts}}{e}}, \quad (20)$$

where only the positive solution of the quadratic expression is physical, as $n_{\rm gr}$ must vanish at $V_{\rm ts}=0$. With Eq. 20, we determined the Dirac point energy as

$$E_{\rm D} = \pm 2e^2 a \sqrt{n_{\rm gr}}.\tag{21}$$

The positive (negative) sign applies to holes (electrons).

The potential difference $V_{\rm ts}$ between the tip and graphene is given by the sum of the applied bias voltage and the contact potential difference between tip and sample surface

$$V_{\rm ts} = V_{\rm s} + V_{\rm CPD} = V_{\rm s} + (\Phi_{\rm tip} - \Phi_{\rm gr})/e$$
 (22)

where the Φ are the respective work functions. While the work function of charge-neutral graphene is well known (see above), the work function of the tip is more difficult to estimate, and critically depends on the details of the tip apex. As a result, for W tips the tip work function can vary in the range $3.9 - 5.5 \,\mathrm{eV}$ [66], but is more typically in the range $4.5 - 5.1 \,\mathrm{eV}$ [11]. We indent our W tips into Au before measurements and expect Au to stick to the tip as a result of the preparation procedure. The work function of bulk Au is $\Phi_{\rm Au} \approx 5.1\,{\rm eV}$, such that we estimate the resulting tip work function to be in the range $\Phi_{\rm tip} = 4.6 - 5.1\,{\rm eV}$, i.e., greater or equal to that of graphene. The fit in Fig. 4b results in a tip work function of $\Phi_{\rm tip} = (4.66 \pm 0.03)\,{\rm eV}$, in excellent agreement with this range of expected values. Our model further compares well with experiments on graphene/NbSe₂ heterostructures ($\Phi_{NbSe_2} \approx 5.6 \, \mathrm{eV}$), where a significant hole doping corresponding to $E_{\rm D} \approx +400\,{\rm meV}$ was reported [67].

Angle-resolved photoemission spectroscopy

Photoemission measurements were performed on cleaved FGT bulk single crystals and were conducted at NanoESCA beamline at Elettra, using the modified Focus GmbH NanoESCA momentum microscope. The sample was cooled using LHe and the temperature was stabilized at $\approx 40\,\mathrm{K}$. The light was incident at an angle 65° with respect to the surface normal, along the K- Γ -K' direction. Extended Data Fig. S12 shows spectra collected at $\hbar\nu=60\,\mathrm{eV}$ in sweep mode with an energy step size of $0.02\,\mathrm{eV}$.

Disentangling band-orbital and chiral-orbital Zeeman effects

We approximate the observed peak shifting behaviour as function of magnetic field by the linear equation system

$$E_1 = g_1 \mu_B B + E_1^0 = (g_z^{CO} - g_z^{BO}) \mu_B B + E_1^0$$
 (23)
 $E_2 = g_2 \mu_B B + E_2^0 = (g_z^{CO} + g_z^{BO}) \mu_B B + E_2^0$, (24)

where $E_i(B)$ are the peak energies, with $E_i^0 \equiv E_i(B=0)$, and $g_z^{\rm CO}$ and $g_z^{\rm BO}$ are the chiral- and band-orbital g-factors , respectively. Inserting the fitted slopes from Fig. 3c, $g_1\mu_{\rm B}=1.8~{\rm meV/T}$ and $g_2\mu_{\rm B}=13.3~{\rm meV/T}$, results in

$$g_z^{\text{BO}} = \frac{g_2 - g_1}{2} \approx 100$$
 (25)

and $g_z^{\rm CO} \approx 130$.

ACKNOWLEDGEMENTS

The authors acknowledge Zhoungqui Lyu for assistance in the lab. Furthermore, the authors are grateful to the Helmholtz Nano Facility for its support regarding sample fabrication. The research was funded by the Deutsche Forschungsgemeinschaft (DFG, German Research Foundation) within the Priority Programme SPP 2244 (project nos. 443416235 and H.B. was supported by the DFG via the project no. PL 712/5-1. Y.M., D.G, M.S. and T.S. acknowledge funding by the DFG in the framework of TRR 288 -422213477 (Project B06), and by the EIC Pathfinder OPEN grant 101129641 "OBELIX". F.L. and F.S.T acknowledge funding from the Bavarian Ministry of Economic Affairs, Regional Development and Energy within Bavaria's High-Tech Agenda Project "Bausteine für das Quantencomputing auf Basis topologischer Materialien mit experimentellen und theoretischen Ansätzen" and Germany's Excellence Strategy -Cluster of Excellence Matter and Light for Quantum Computing (ML4Q) through an Independence Grant. J.M.C. acknowledges funding from the Alexander von Humboldt Foundation. M.T. acknowledges support from the Heisenberg Program (Grant No. TE 833/2-1) of the DFG.

Author contributions F.L. conceived the project. T.W. and H.B. fabricated samples. T.W. and F.L. designed the STM experiment and acquired the data, which were analyzed by T.W., M.T. and F.L. M.S., T.G.S., D.G. and Y.M. performed DFT calculations. T.W. and S.L. performed auxillary calculations. F.L. performed the capacitor circuit calculations. H.B. and L.P. designed the ARPES experiment, acquired, and analyzed the corresponding data. L.P., Y.M., M.T., F.S.T. and F.L. supervised the project. T.W., J.M.C., F.S.T. and F.L. wrote the manuscript, and all authors commented on the manuscript.

Competing financial interests The authors declare no competing financial interests.

REFERENCES

- N. Armitage, E. Mele, and A. Vishwanath, Weyl and Dirac semimetals in three-dimensional solids, Reviews of Modern Physics 90, 015001 (2018).
- [2] X. Wan, A. M. Turner, A. Vishwanath, and S. Y. Savrasov, Topological semimetal and fermi-arc surface states in the electronic structure of pyrochlore iridates, Physical Review B 83, 205101 (2011).
- [3] Y. Machida, S. Nakatsuji, S. Onoda, T. Tayama, and T. Sakakibara, Time-reversal symmetry breaking and spontaneous Hall effect without magnetic dipole order, Nature 463, 210 (2010).
- [4] Y. Tokura, K. Yasuda, and A. Tsukazaki, Magnetic topological insulators, Nature Reviews Physics 1, 126 (2019).
- [5] B. Chen, J. Yang, H. Wang, M. Imai, H. Ohta, C. Michioka, K. Yoshimura, and M. Fang, Magnetic properties of layered itinerant electron ferromagnet Fe₃GeTe₂, Journal of the Physical Society of Japan 82, 124711 (2013).
- [6] S. W. Jang, H. Yoon, M. Y. Jeong, S. Ryee, H.-S. Kim, and M. J. Han, Origin of ferromagnetism and the effect of doping on Fe₃GeTe₂, Nanoscale 12, 13501 (2020).

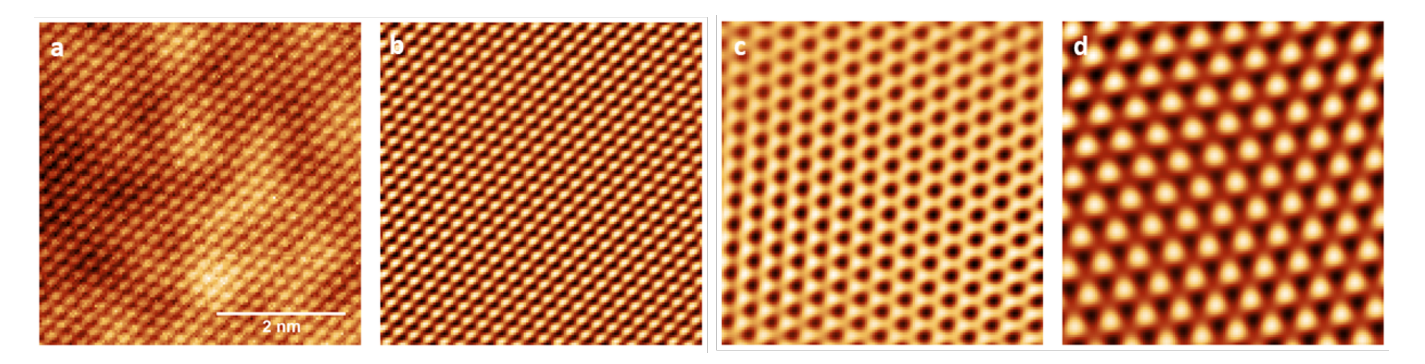
- [7] J.-X. Zhu, M. Janoschek, D. Chaves, J. Cezar, T. Durakiewicz, F. Ronning, Y. Sassa, M. Mansson, B. Scott, N. Wakeham, et al., Electronic correlation and magnetism in the ferromagnetic metal Fe₃GeTe₂, Physical Review B 93, 144404 (2016).
- [8] Y. Zhang, H. Lu, X. Zhu, S. Tan, W. Feng, Q. Liu, W. Zhang, Q. Chen, Y. Liu, X. Luo, *et al.*, Emergence of Kondo lattice behavior in a van der Waals itinerant ferromagnet, Fe₃GeTe₂, Science Advances 4, eaao6791 (2018).
- [9] T. J. Kim, S. Ryee, and M. J. Han, Fe₃GeTe₂: a site-differentiated Hund metal, npj Computational Materials 8, 245 (2022).
- [10] K. Kim, J. Seo, E. Lee, K.-T. Ko, B. Kim, B. G. Jang, J. M. Ok, J. Lee, Y. J. Jo, W. Kang, *et al.*, Large anomalous Hall current induced by topological nodal lines in a ferromagnetic van der Waals semimetal, Nature Materials 17, 794 (2018).
- [11] M. Zhao, Y. Zhao, Y. Xi, H. Xu, H. Feng, X. Xu, W. Hao, S. Zhou, J. Zhao, S. X. Dou, et al., Electric-field-driven negative differential conductance in 2D van der Waals ferromagnet Fe₃GeTe₂, Nano Letters 21, 9233 (2021).
- [12] M. Zhao, B.-B. Chen, Y. Xi, Y. Zhao, H. Xu, H. Zhang, N. Cheng, H. Feng, J. Zhuang, F. Pan, et al., Kondo holes in the two-dimensional itinerant ising ferromagnet Fe₃GeTe₂, Nano Letters 21, 6117 (2021).
- [13] P. K. Srivastava, Y. Hassan, S. Lee, M. Joe, M. S. Abbas, H. Ahn, A. Tiwari, S. Ghosh, W. J. Yoo, B. Singh, *et al.*, Unusual Dzyaloshinskii-Moriya interaction in graphene/Fe₃GeTe₂ van der Waals heterostructure, Small **20**, 2402604 (2024).
- [14] Y. Deng, Y. Yu, Y. Song, J. Zhang, N. Z. Wang, Z. Sun, Y. Yi, Y. Z. Wu, S. Wu, J. Zhu, et al., Gate-tunable room-temperature ferromagnetism in two-dimensional Fe₃GeTe₂, Nature 563, 94 (2018).
- [15] X. Wang, J. Tang, X. Xia, C. He, J. Zhang, Y. Liu, C. Wan, C. Fang, C. Guo, W. Yang, *et al.*, Current-driven magnetization switching in a van der Waals ferromagnet Fe₃GeTe₂, Science Advances 5, eaaw8904 (2019).
- [16] S. Y. Park, D. S. Kim, Y. Liu, J. Hwang, Y. Kim, W. Kim, J.-Y. Kim, C. Petrovic, C. Hwang, S.-K. Mo, *et al.*, Controlling the magnetic anisotropy of the van der Waals ferromagnet Fe₃GeTe₂ through hole doping, Nano Letters **20**, 95 (2019).
- [17] R. Shindou and N. Nagaosa, Orbital ferromagnetism and anomalous Hall effect in antiferromagnets on the distorted fcc lattice, Physical Review Letters 87, 116801 (2001).
- [18] G. Tatara and N. Garcia, Quantum toys for quantum computing: Persistent currents controlled by the spin Josephson effect, Physical Review Letters 91, 076806 (2003).
- [19] L. Bulaevskii, C. Batista, M. Mostovoy, and D. Khomskii, Electronic orbital currents and polarization in Mott insulators, Physical Review B 78, 024402 (2008).
- [20] M. dos Santos Dias, J. Bouaziz, M. Bouhassoune, S. Blügel, and S. Lounis, Chirality-driven orbital magnetic moments as a new probe for topological magnetic structures, Nature Communications 7, 13613 (2016).
- [21] B. Zhao, B. Karpiak, A. M. Hoque, P. Dhagat, and S. P. Dash, Strong perpendicular anisotropic ferromagnet Fe₃GeTe₂/graphene van der Waals heterostructure, Journal of Physics D: Applied Physics 56, 094001 (2023).
- [22] J.-P. Hanke, F. Freimuth, A. K. Nandy, H. Zhang, S. Blügel, and Y. Mokrousov, Role of Berry phase theory for describing orbital magnetism: From magnetic heterostructures to topological orbital ferromagnets, Physical Review B 94, 121114 (2016).
- [23] J.-X. Yin, S. S. Zhang, H. Li, K. Jiang, G. Chang, B. Zhang, B. Lian, C. Xiang, I. Belopolski, H. Zheng, *et al.*, Giant and anisotropic many-body spin-orbit tunability in a strongly correlated Kagome magnet, Nature **562**, 91 (2018).

- [24] F. R. Lux, F. Freimuth, S. Blügel, and Y. Mokrousov, Engineering chiral and topological orbital magnetism of domain walls and skyrmions, Communications Physics 1, 60 (2018).
- [25] S. Grytsiuk, J.-P. Hanke, M. Hoffmann, J. Bouaziz, O. Gomonay, G. Bihlmayer, S. Lounis, Y. Mokrousov, and S. Blügel, Topological-chiral magnetic interactions driven by emergent orbital magnetism, Nature Communications 11, 511 (2020).
- [26] H. Li, H. Zhao, K. Jiang, Q. Wang, Q. Yin, N.-N. Zhao, K. Liu, Z. Wang, H. Lei, and I. Zeljkovic, Manipulation of Dirac band curvature and momentum-dependent g-factor in a Kagome magnet, Nature Physics 18, 644 (2022).
- [27] I. Lima Fernandes and S. Lounis, Universal patterns of skyrmion magnetizations unveiled by defect implantation, arXiv:2312.05903 (2023).
- [28] Z. Fei, B. Huang, P. Malinowski, W. Wang, T. Song, J. Sanchez, W. Yao, D. Xiao, X. Zhu, A. F. May, *et al.*, Two-dimensional itinerant ferromagnetism in atomically thin Fe₃GeTe₂, Nature Materials 17, 778 (2018).
- [29] R. Decker, Y. Wang, V. W. Brar, W. Regan, H.-Z. Tsai, Q. Wu, W. Gannett, A. Zettl, and M. F. Crommie, Local electronic properties of graphene on a BN substrate via scanning tunneling microscopy, Nano Letters 11, 2291 (2011).
- [30] Y. Zhang, V. W. Brar, F. Wang, C. Girit, Y. Yayon, M. Panlasigui, A. Zettl, and M. F. Crommie, Giant phonon-induced conductance in scanning tunnelling spectroscopy of gatetunable graphene, Nature Physics 4, 627 (2008).
- [31] F. D. Natterer, Y. Zhao, J. Wyrick, Y.-H. Chan, W.-Y. Ruan, M.-Y. Chou, K. Watanabe, T. Taniguchi, N. B. Zhitenev, and J. A. Stroscio, Strong asymmetric charge carrier dependence in inelastic electron tunneling spectroscopy of graphene phonons, Physical Review Letters 114, 245502 (2015).
- [32] Z. Qiu, M. Holwill, T. Olsen, P. Lyu, J. Li, H. Fang, H. Yang, M. Kashchenko, K. S. Novoselov, and J. Lu, Visualizing atomic structure and magnetism of 2D magnetic insulators via tunneling through graphene, Nature Communications 12, 1 (2021).
- [33] L. Sun, L. Rademaker, D. Mauro, A. Scarfato, Á. Pásztor, I. Gutiérrez-Lezama, Z. Wang, J. Martinez-Castro, A. F. Morpurgo, and C. Renner, Determining spin-orbit coupling in graphene by quasiparticle interference imaging, Nature Communications 14, 3771 (2023).
- [34] H. Li, S. Cheng, G. Pokharel, P. Eck, C. Bigi, F. Mazzola, G. Sangiovanni, S. D. Wilson, D. Di Sante, Z. Wang, *et al.*, Spin Berry curvature-enhanced orbital Zeeman effect in a Kagome metal, Nature Physics 20, 1103 (2024).
- [35] W. Yao, D. Xiao, and Q. Niu, Valley-dependent optoelectronics from inversion symmetry breaking, Physical Review B 77, 235406 (2008).
- [36] D. Jo, D. Go, Y. Mokrousov, P. M. Oppeneer, S.-W. Cheong, and H.-W. Lee, Weak ferromagnetism in altermagnets from alternating *g*-Tensor anisotropy, Physical Review Letters **134**, 196703 (2025).
- [37] S. Mühlbauer, B. Binz, F. Jonietz, C. Pfleiderer, A. Rosch, A. Neubauer, R. Georgii, and P. Böni, Skyrmion lattice in a chiral magnet, Science 323, 915 (2009).
- [38] D. Li, S. Haldar, T. Drevelow, and S. Heinze, Tuning the magnetic interactions in van der Waals Fe₃GeTe₂ heterostructures: A comparative study of ab initio methods, Physical Review B 107, 104428 (2023).
- [39] C. Niu, J.-P. Hanke, P. M. Buhl, H. Zhang, L. Plucinski, D. Wortmann, S. Blügel, G. Bihlmayer, and Y. Mokrousov, Mixed topological semimetals driven by orbital complexity in two-dimensional ferromagnets, Nature Communications 10, 3179 (2019).

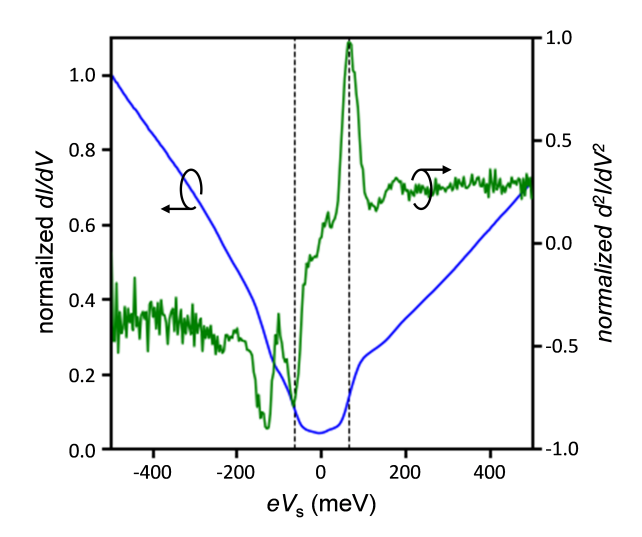
- [40] E. Ko, Hybridized bands and stacking-dependent band edges in ferromagnetic Fe₃GeTe₂/CrGeTe₃ moiré heterobilayer, Scientific reports 12, 1 (2022).
- [41] Y.-J. Yu, Y. Zhao, S. Ryu, L. E. Brus, K. S. Kim, and P. Kim, Tuning the graphene work function by electric field effect, Nano Letters 9, 3430 (2009).
- [42] S. Huang, L. Zhu, Y. Zhao, K. Watanabe, T. Taniguchi, J. Xiao, L. Wang, J. Mei, H. Huang, F. Zhang, *et al.*, Giant magnetoresistance induced by spin-dependent orbital coupling in Fe₃GeTe₂/graphene heterostructures, Nature Communications 16, 2866 (2025).
- [43] K. S. Kim, T.-H. Kim, A. L. Walter, T. Seyller, H. W. Yeom, E. Rotenberg, and A. Bostwick, Visualizing atomic-scale negative differential resistance in bilayer graphene, Physical Review Letters 110, 036804 (2013).
- [44] A. Luican-Mayer, Y. Zhang, A. DiLullo, Y. Li, B. Fisher, S. E. Ulloa, and S.-W. Hla, Negative differential resistance observed on the charge density wave of a transition metal dichalcogenide, Nanoscale 11, 22351 (2019).
- [45] L.-J. Yin, L.-Z. Yang, L. Zhang, Q. Wu, X. Fu, L.-H. Tong, G. Yang, Y. Tian, L. Zhang, and Z. Qin, Imaging of nearly flat band induced atomic-scale negative differential conductivity in ABC-stacked trilayer graphene, Physical Review B 102, 241403 (2020).
- [46] M. García-Díez, H. Beidenkopf, I. Robredo, and M. G. Vergniory, Origins of the anomalous Hall conductivity in the symmetry enforced Fe₃GeTe₂ nodal-line ferromagnet, Journal of Physics: Materials 8, 035012 (2025).
- [47] B. C. Sales, J. Yan, W. R. Meier, A. D. Christianson, S. Okamoto, and M. A. McGuire, Electronic, magnetic, and thermodynamic properties of the Kagome layer compound FeSn, Physical Review Materials 3, 114203 (2019).
- [48] J.-X. Yin, S. S. Zhang, G. Chang, Q. Wang, S. S. Tsirkin, Z. Guguchia, B. Lian, H. Zhou, K. Jiang, I. Belopolski, *et al.*, Negative flat band magnetism in a spin–orbit-coupled correlated Kagome magnet. Nature Physics 15, 443 (2019).
- [49] Y. Xing, J. Shen, H. Chen, L. Huang, Y. Gao, Q. Zheng, Y.-Y. Zhang, G. Li, B. Hu, G. Qian, *et al.*, Localized spin-orbit polaron in magnetic Weyl semimetal Co₃Sn₂S₂, Nature Communications 11, 5613 (2020).
- [50] Z. Ren, H. Li, S. Sharma, D. Bhattarai, H. Zhao, B. Rachmilowitz, F. Bahrami, F. Tafti, S. Fang, M. P. Ghimire, *et al.*, Plethora of tunable Weyl fermions in Kagome magnet Fe₃Sn₂ thin films, npj Quantum Materials 7, 109 (2022).
- [51] For the program description, see "https://www.flapw.de" (accessed 2025/10/28).
- [52] E. Wimmer, H. Krakauer, M. Weinert, and A. J. Freeman, Full-potential self-consistent linearized-augmented-plane-wave method for calculating the electronic structure of molecules and surfaces: O₂ molecule, Physical Review B 24, 864 (1981).
- [53] J. P. Perdew, K. Burke, and M. Ernzerhof, Generalized gradient approximation made simple, Physical Review Letters 77, 3865 (1996)
- [54] https://materials.springer.com/isp/crystallographic/docs/ sd_1420956 (accessed 2025/10/28).
- [55] X. Wang, J. R. Yates, I. Souza, and D. Vanderbilt, Ab initio calculation of the anomalous Hall conductivity by Wannier interpolation, Physical Review B 74, 195118 (2006).
- [56] G. Pizzi, V. Vitale, R. Arita, S. Blügel, F. Freimuth, G. Géranton, M. Gibertini, D. Gresch, C. Johnson, T. Koretsune, et al., Wannier90 as a community code: new features and applications, Journal of Physics: Condensed Matter 32, 165902 (2020).

- [57] F. Freimuth, Y. Mokrousov, D. Wortmann, S. Heinze, and S. Blügel, Maximally localized Wannier functions within the FLAPW formalism, Physical Review B 78, 035120 (2008).
- [58] M. Lopez, D. Vanderbilt, T. Thonhauser, and I. Souza, Wannier-based calculation of the orbital magnetization in crystals, Physical Review B 85, 014435 (2012).
- [59] H.-H. Yang, N. Bansal, P. Rüßmann, M. Hoffmann, L. Zhang, D. Go, Q. Li, A.-A. Haghighirad, K. Sen, S. Blügel, et al., Magnetic domain walls of the van der Waals material Fe₃GeTe₂, 2D Materials 9, 025022 (2022).
- [60] T. G. Saunderson, D. Go, S. Blügel, M. Kläui, and Y. Mokrousov, Hidden interplay of current-induced spin and orbital torques in bulk Fe₃GeTe₂, Physical Review Research 4, L042022 (2022).
- [61] Y. Wakafuji, R. Moriya, S. Masubuchi, K. Watanabe, T. Taniguchi, and T. Machida, 3D manipulation of 2D materials using microdome polymer, Nano Letters 20, 2486 (2020).
- [62] C. T. Black and J. J. Welser, Electric-field penetration into metals: consequences for high-dielectric-constant capacitors, IEEE Transactions on Electron Devices 46, 776 (1999).
- [63] A. Ambrosetti and P. L. Silvestrelli, Faraday-like screening by two-dimensional nanomaterials: A scale-dependent tunable effect, The Journal of Physical Chemistry Letters 10, 2044 (2019).
- [64] F. Lüpke, S. Just, M. Eschbach, T. Heider, E. Młyńczak, M. Lanius, P. Schüffelgen, D. Rosenbach, N. von den Driesch, V. Cherepanov, et al., In situ disentangling surface state transport channels of a topological insulator thin film by gating, npj Quantum Materials 3, 46 (2018).
- [65] J. Xia, F. Chen, J. Li, and N. Tao, Measurement of the quantum capacitance of graphene, Nature Nanotechnology 4, 505 (2009).
- [66] A. Wijnheijmer, J. Garleff, M. vd Heijden, and P. Koenraad, Influence of the tip work function on scanning tunneling microscopy and spectroscopy on zinc doped GaAs, Journal of Vacuum Science & Technology B, Nanotechnology and Microelectronics: Materials, Processing, Measurement, and Phenomena 28, 1086 (2010).
- [67] Y. Chen, L. Wu, H. Xu, C. Cong, S. Li, S. Feng, H. Zhang, C. Zou, J. Shang, S. A. Yang, K. P. Loh, W. Huang, and T. Yu, Visualizing the anomalous charge density wave states in graphene/NbSe₂ heterostructures, Advanced Materials 32, 2003746 (2020).

EXTENDED DATA



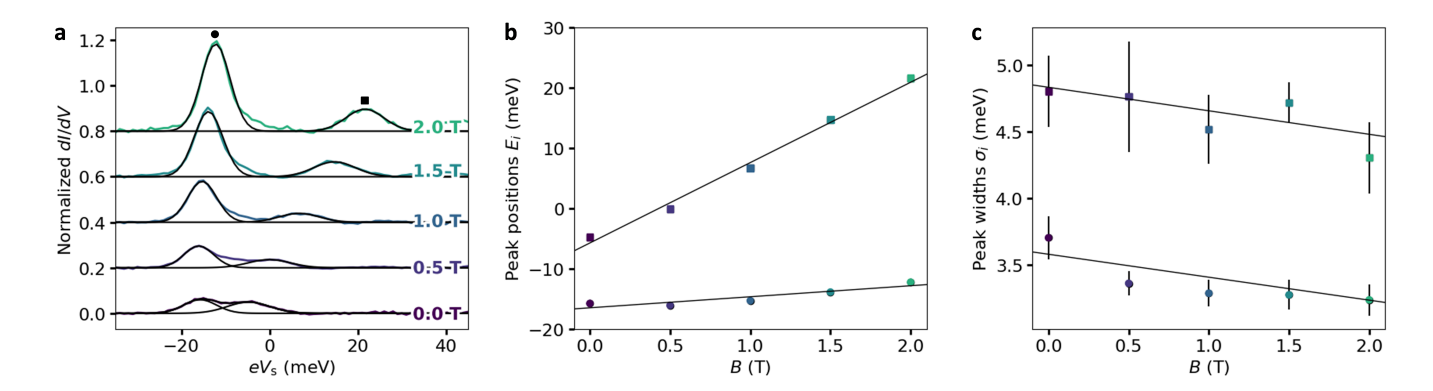
Extended Data Fig. S1. Fourier-filtered topography of graphene, Fe_3GeTe_2 and their moiré lattice. (a) STM topography (constant-current image at $V_s = -50 \,\mathrm{mV}$, $I_t = 70 \,\mathrm{pA}$), measured on the heterostructure shown in Fig. 2a (b) Fourier-filtered graphene lattice. (c) Fourier-filtered Fe₃GeTe₂ lattice. (d) Fourier-filtered moiré lattice. The images in panels b to d were generated by inverse FFT of the Fourier transform image of panel a, selecting only the corresponding spots, as marked by the black, orange and red circles in Fig. 2b, respectively.



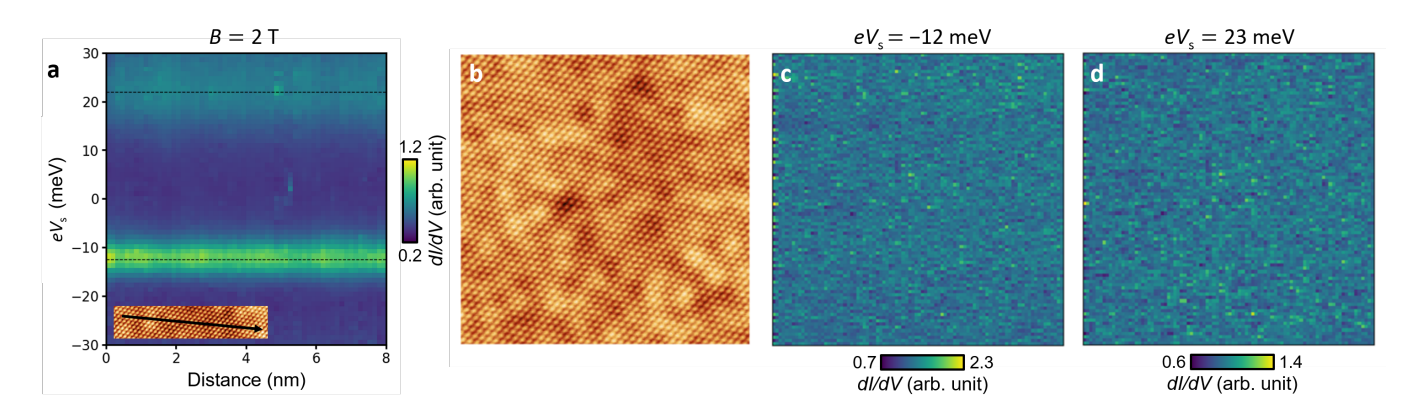
Extended Data Fig. S2. Threshold determination of the inelastic tunnelling gap of graphene. Differential conductance spectrum (blue curve, arbitrary units) measured on the graphene/Fe₃GeTe₂ heterostructure shown in Fig. 2a ($V_{\rm s}=500\,{\rm mV}$, $I_{\rm t}=200\,{\rm pA}$), and numerically differentiated ${\rm d}^2I/{\rm d}V^2$ curve (green, arbitrary units). The leading peaks and dips of the second derivative (vertical dashed lines) were used to determine the thresholds of the inelastic tunnelling gap as $|eV_{\rm s}|=\hbar\omega=(65\pm2)\,{\rm meV}$, corresponding to the out-of-plane acoustic phonon of graphene [31].

I_{t} (nA)	δh (Å)	$C_{\rm tip}(\mu { m Fcm}^{-2})$	$E_{\rm D}$ (meV)	$n_{\rm gr} (10^{10} {\rm cm}^{-2})$	$E_{\rm FGT}$ (GV/m)
0.1	0	0.885	-38.7 ± 2.6	5.50 ± 0.74	1.291 ± 0.008
0.3	0.500	0.932	-33.6 ± 2.6	4.15 ± 0.64	1.306 ± 0.008
0.5	0.732	0.955	-30.5 ± 2.2	3.42 ± 0.49	1.316 ± 0.007
0.8	0.946	0.978	-26.5 ± 2.7	2.58 ± 0.53	1.328 ± 0.008
1.0	1.048	0.989	-27.8 ± 2.4	2.84 ± 0.49	1.324 ± 0.007

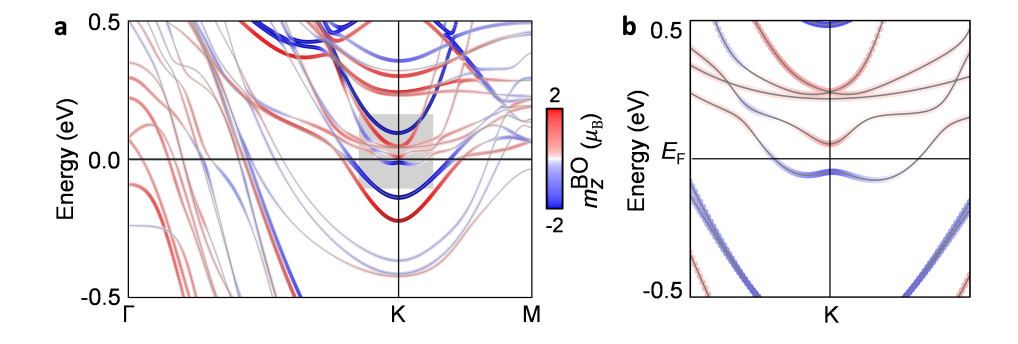
Extended Data Table I. Change in tip height δh , tip-graphene capacitance $C_{\rm tip}$ (Eq. 10), Dirac point energy $E_{\rm D}$ (Fig. 4a), charge carrier concentration (Eq. 21), and interface electric field $E_{\rm FGT}$ (Eq. 1), all as a function of setpoint tunnel current $I_{\rm t}$.



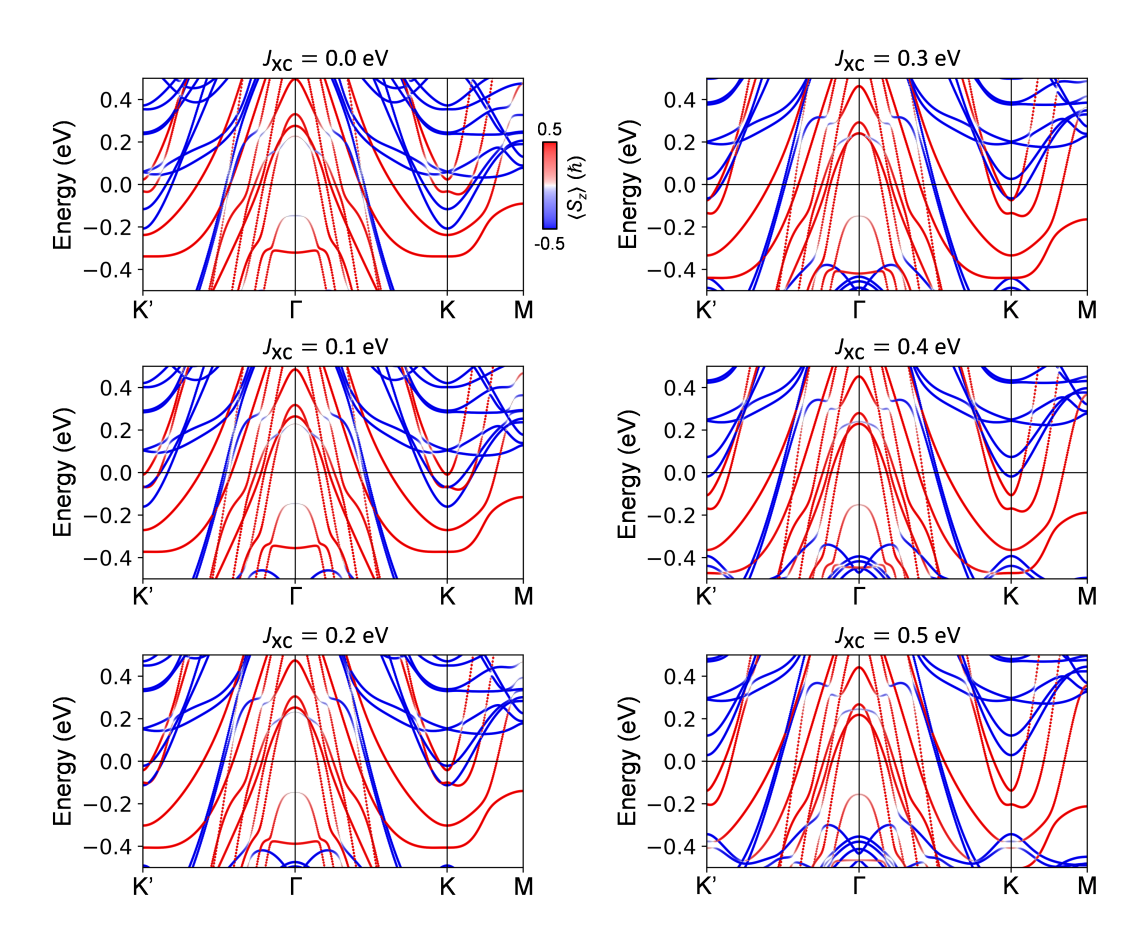
Extended Data Fig. S3. Fit results for the two Fe₃GeTe₂-related peaks in the inelastic tunnelling gap of graphene, as a function of external B field. (a) Differential conductance spectra (arbitrary units) after subtraction of a polynomial background (colored data curves, same data set as in Fig. 3b). The displayed Gaussians $A_i e^{-(eV_s - E_i)^2/2\sigma_i^2}$ (black curves) were fitted to the data separately for each curve and peak, except at B = 0, where because of their significant overlap the two peaks were fitted simultaneously . (b, c) Fitted peak energies E_i and widths σ_i , respectively, with linear fits for each peak.



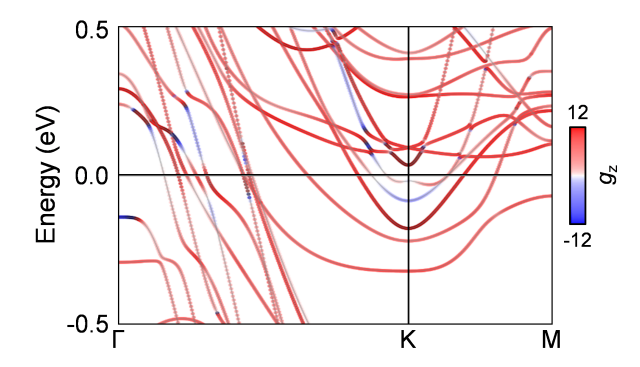
Extended Data Fig. S4. Spatial consistency of the two Fe₃GeTe₂-related peaks at B=2 T. (a) Color map of differential conductance spectra (arbitrary units), recorded at positions along the arrow in the STM topography in the inset The map reveals constant peak energies and intensities. (b) STM topography recorded at another position on the graphene/Fe₃GeTe₂ heterostructure. Scan size: 10 nm. (c, d) Color maps of differential conductance spectra (arbitrary units) recorded in the area shown in panel b at the two peak energies marked by dotted lines in panel a. No spatial variations, for example due to scattering at defects, are discernible. Tip stabilization parameters for all panels: $V_s = 50$ mV, $I_t = 1$ nA.



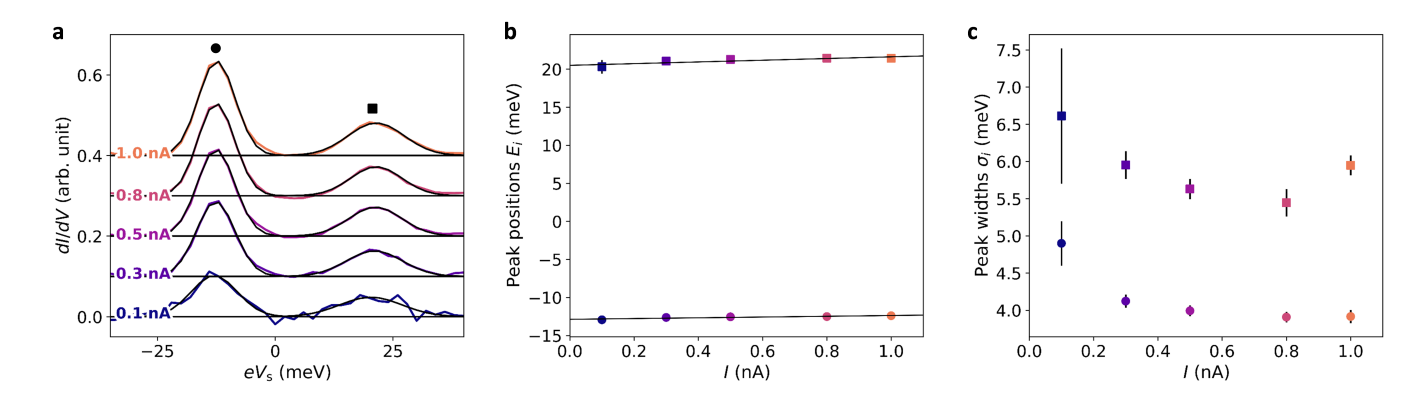
Extended Data Fig. S5. **DFT-calculated band structure of trilayer Fe_3GeTe_2.** (a) In Fe_3GeTe_2 trilayers, the inversion symmetry of bulk Fe_3GeTe_2 (bilayer unit cell) is broken. This leads to additional bands close to E_F , a smaller nodal line gap, and smaller band orbital moments (color coded). Furthermore, the K and K' points are no longer equivalent, although their differences are minimal. We thus only show the K point here. The band structure in this panel should be compared with Fig. 1c, which was calculated for bulk Fe_3GeTe_2 . We note that the band crossing at K/K' does not exist in monolayer FGT. However, the spin canting, which is strongest in the layer closest to the interface (compare Fig. 1e) may break inversion symmetry for two or more FGT layers and thus can explain a smaller gap at K/K'. (b) Zoom into the shaded region in panel a, showing the bands close to the K point.



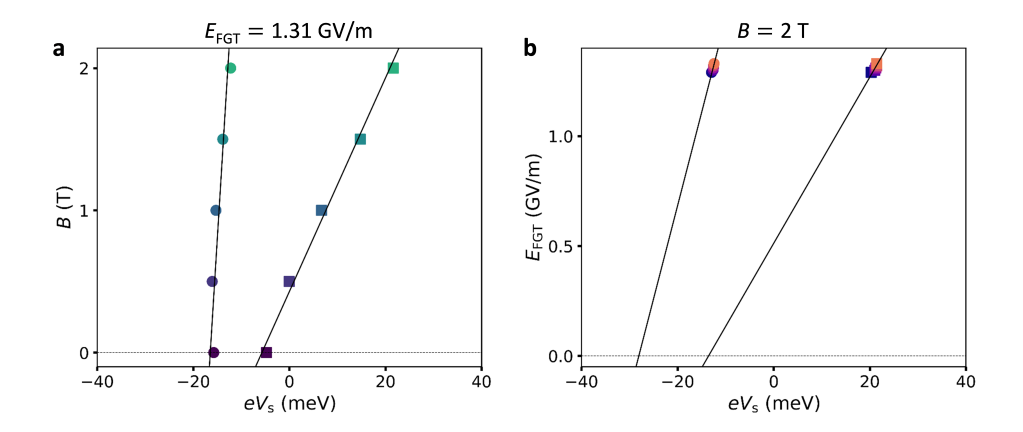
Extended Data Fig. S6. **Fe**₃**GeTe**₂ **band structure as a function of magnetic exchange potential strength.** To model the spin Zeeman effect in an external magnetic field, we took the DFT-calculated single-particle band structure of Fe₃GeTe₂ (see Fig. 1c) and added exchange coupling of varying size, ranging from $J_{xc} = 0$ to $0.5 \, \mathrm{eV}$. The additional exchange coupling is added on top of the FGT Wannier Hamiltonian by using the matrix elements of the spin operator in terms of Wannier functions.



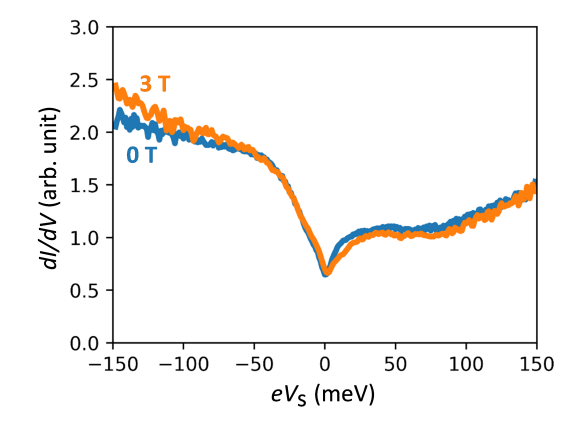
Extended Data Fig. S7. Calculated out-of-plane g-factor, neglecting the influence of spin canting and chiral orbital moments. The plot shows the band structure of Fig. 1c, with color-coded $g_z^{\rm BO} = 2 + \langle L \rangle/\langle S \rangle$ resulting from the spin and orbital moments shown as color-coding in Fig. 1c and d, respectively.



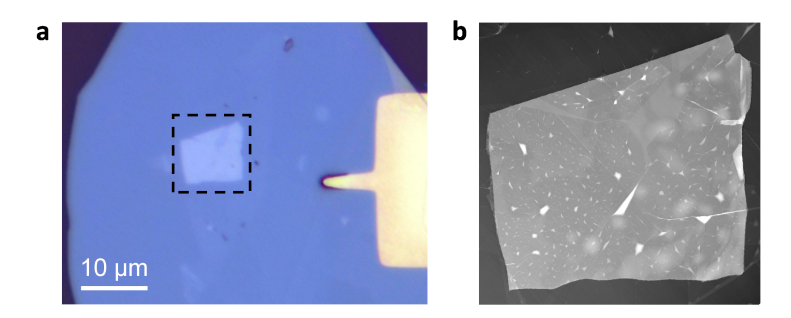
Extended Data Fig. S8. Fit results for the two Fe₃GeTe₂-related peaks in the inelastic tunnelling gap of graphene, as function of setpoint current. (a) Differential conductance spectra (arbitrary units, measured at $B=2\,\mathrm{T}$) after subtraction of a polynomial background (colored data curves, same data set as in Fig. 4c). The displayed Gaussians $A_i e^{-(eV_s-E_i)^2/2\sigma_i^2}$ (black curves) were fitted to the data separately for each curve and peak. (b, c) Fitted peak energies E_i and widths σ_i , respectively, with linear fits in panel b for each of the two peaks.



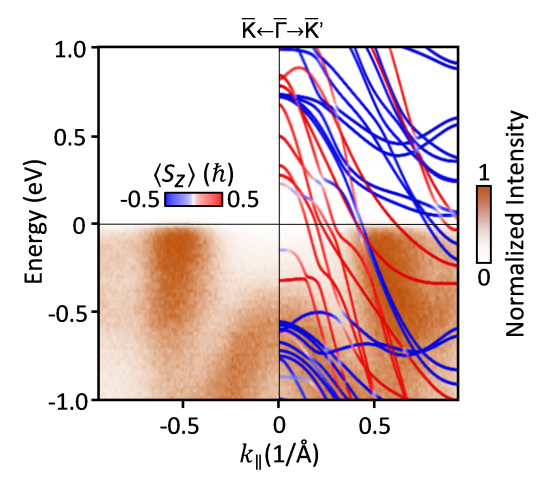
Extended Data Fig. S9. Fitted peak positions for the two Fe₃GeTe₂-related peaks in the inelastic tunnelling gap of graphene, as function of magnetic and electric field. (a) B-field-dependent Zeeman effect at $E_{\rm FGT}=1.31\,{\rm GV/m}$. Data points and linear fits (solid lines) are the same as in Fig. 3c. (b) $E_{\rm FGT}$ -field-dependent Zeeman effect at $B=2\,{\rm T}$. Data points and linear fits (solid lines) are the same as in Fig. 4d.



Extended Data Fig. S10. Differential conductance spectra of bulk Fe_3GeTe_2 . No significant change is observed as a function of applied magnetic field up to our maximum field of B=3 T. The data is consistent with previous reports in the literature [11, 12] and confirms that breaking of inversion symmetry at the interface is a necessary condition to observe the specific behavior of spectral features reported in the main text.



Extended Data Fig. S11. Atomic force microscopy on the the graphene/ Fe_3GeTe_2 heterostructure. (a) Optical micrograph of the heterostructure (same as in Fig. 1e), with the black dashed line representing the outline of the AFM measurement in panel b. (b) Atomic force micrograph of the graphene-covered Fe_3GeTe_2 flake. The formation of 'dirt pockets' indicates an atomically clean vdW interface in between the pockets, in consistency with the spatially uniform STM measurements that were performed in different spots on the sample.



Extended Data Fig. S12. Angle-resolved photoemission spectroscopy of bulk Fe₃GeTe₂. The experimental photoemission data (band maps from $\bar{\Gamma}$ to \bar{K} on the left and $\bar{\Gamma}$ to \bar{K}' on the right) are overlayed with the DFT-calculated band structure including SOC (from Fig. 1c) in $\bar{\Gamma}K$ direction. Red and blue bands correspond to the majority (minority) spins.